



Brittle-to-ductile transitions in glasses: Roles of soft defects and loading geometry

David Richard¹, Edan Lerner^{2*}, and Eran Bouchbinder^{3*}

Glasses are non-crystalline materials that find an enormous range of industrial and technological applications. They are typically formed by rapidly cooling liquids, resulting in arrested out-of-equilibrium states lacking the long-range order of their crystalline counterparts. The emerging disordered structures, which vary with the formation cooling rate, give rise to large variability in material properties. Among these, the fracture toughness — quantifying materials' ability to resist catastrophic failure in the presence of a crack — is of prime importance; understanding its physical origin and range of variability is a major challenge with far-reaching implications. To address this challenge, we employ cutting-edge and extensive computer simulations of glasses, spanning a range of material properties that is comparable to that of real-life glasses. We focus on the failure resistance and show that it is controlled by both the abundance of soft defects inside the glass, which are responsible for glasses' plastic deformability, and by the loading configuration of the fracture test employed, which affects the imposed deformation geometry. These two physical factors control together a transition from ductile-like (gradual, accompanied by extensive plastic deformation) failure to brittle-like (abrupt, accompanied by little and localized plastic deformation) failure.

Understanding the fracture toughness of glasses is of prime importance for science and technology. We study it here using extensive atomistic simulations in which the interaction potential, glass transition cooling rate, and loading geometry are systematically varied, mimicking a broad range of experimentally accessible properties. Glasses' non-equilibrium mechanical disorder is quantified through A_g , the dimensionless prefactor of the universal spectrum of non-phononic excitations, which measures the abundance of soft glassy defects that affect plastic deformability. We show that while a brittle-to-ductile transition might be induced by reducing the cooling rate, leading to a reduction in A_g , iso- A_g glasses are either brittle or ductile depending on the degree of Poisson contraction under unconstrained uniaxial tension. Eliminating Poisson contraction using constrained tension reveals that iso- A_g glasses feature similar toughness, and that varying A_g under these conditions results in significant toughness variation. Our results highlight the roles played by both soft defects and loading geometry (which affects the activation of defects) in the toughness of glasses.

Introduction

Glasses are intrinsically non-equilibrium materials whose properties may vary vastly with their thermomechanical history (e.g., the cooling rate at which they are formed from a melt).¹ The non-equilibrium nature of glasses is mesoscopically manifested through a broad range of disordered structures, which qualitatively differ from the corresponding ordered structures featured by their crystalline counterparts. Macroscopically, the non-equilibrium nature of glasses may be manifested in a substantial variability in various material properties, even for the very same composition.

One such important material property is the ability of a glass to resist catastrophic failure. The latter is commonly quantified by the fracture toughness, which measures the material resistance to failure in the presence of an initial crack.² The value of the fracture toughness reflects a multitude of spatiotemporal processes that take place in the material prior to catastrophic failure. In one limit, failure is accompanied by rather localized plastic deformation (**Figure 1a**, right) and is generally quite abrupt. The fracture toughness is typically small in this case, and failure is commonly termed *brittle-like*. In the opposite limit,

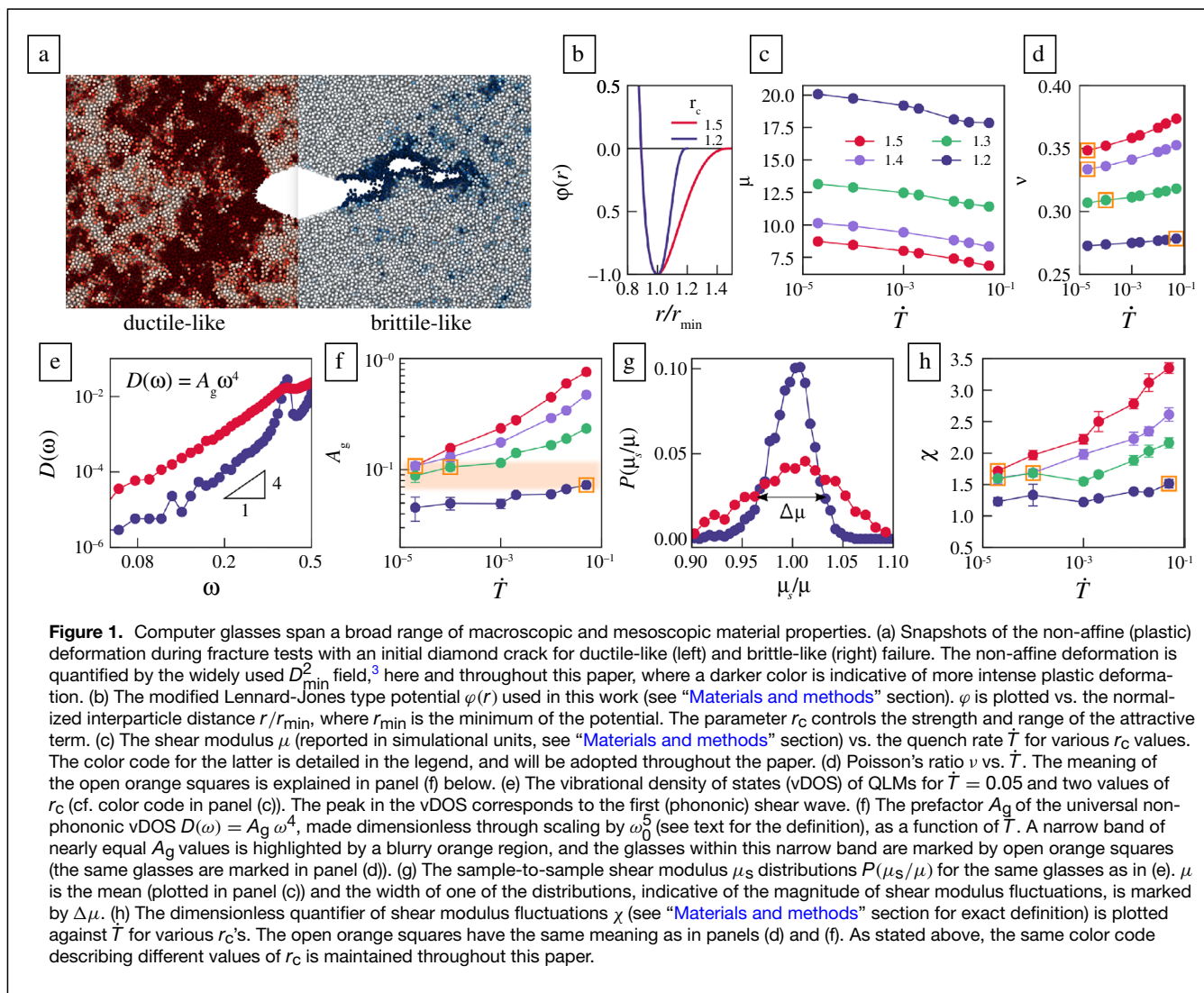
David Richard, Institute of Theoretical Physics, University of Amsterdam, Science Park 904, 1098 XH Amsterdam, The Netherlands; d.richard@uva.nl

Edan Lerner, Institute of Theoretical Physics, University of Amsterdam, Science Park 904, 1098 XH Amsterdam, The Netherlands; e.lerner@uva.nl

Eran Bouchbinder, Chemical and Biological Physics Department, Weizmann Institute of Science, 7610001 Rehovot, Israel; eran.bouchbinder@weizmann.ac.il

*Corresponding authors

doi:10.1557/s43577-021-00171-8



failure is accompanied by significant spatially extended plastic deformation (Figure 1a, left) and is generally more gradual. The fracture toughness is typically larger in this case, and failure is commonly termed *ductile-like*.

Understanding the transition between these two modes of failure is an important challenge in materials science.^{4–9} Establishing, understanding, and predicting structure–dynamics–properties relations in glasses (e.g., in the context of material failure), involve various challenges. First, one should develop tools to quantify the disordered structures featured by glasses. Second, one should identify a certain sub-class of structural degrees of freedom that is relevant for a given macroscopic material property. Third, one should understand the dynamic evolution of these relevant degrees of freedom under some prescribed conditions. Finally, one should be able to coarse-grain over mesoscopic structural degrees of freedom in order to understand how collective dynamics control the macroscopic material property.

Quantifying mesoscopic structural and mechanical disorder in glasses is challenging. One aspect of the challenge

is that we generally lack tools and concepts to distinguish one disordered state from another, in sharp contrast to well-established “order parameters” in other condensed-matter systems.¹⁰ Another aspect of the challenge is the associated length scales; glassy disorder typically manifests itself on small length scales, usually corresponding to a few atomic distances, which are not directly accessible to currently available experimental techniques in molecular glasses. Consequently, computer glasses—where such length scales are readily accessible—have played important roles in our understanding of glassy disorder.^{11–14}

Recently, computer studies revealed and substantiated the existence of low-frequency (soft) non-phononic vibrational modes in glasses.^{14–21} These soft vibrational modes (or excitations) have been shown to be quasilocated in space,^{16,17,22} as opposed to the spatially extended nature of low-frequency phonons (i.e., plane waves), hence they are termed hereafter quasilocated modes (QLMs). Moreover, QLMs have been shown to follow a universal vibrational density of



states (vDOS) $\mathcal{D}(\omega) \sim \omega^4$, where ω is the angular vibrational frequency^{14,15,19,20, 23–28} (examples in Figure 1e). As the ω^4 law is universal (i.e., independent of the glass composition, interatomic interactions, and dimensionality) all of the glass history dependence is encapsulated in the non-universal prefactor A_g , defined through $\mathcal{D}(\omega) \equiv A_g \omega^4$. A_g , once properly non-dimensionalized (see next), has been shown to provide a measure of the number density of QLMs in a glass.^{14,15,26,29,30}

QLMs, in turn, have been shown to correlate with the spatial loci of irreversible rearrangements in glasses (i.e., they statistically correlate with shear transformation zones (STZs), the carriers of plasticity in glassy materials).^{18,21,31–36} As such, the properly non-dimensionalized A_g is directly relevant for plastic deformability, and consequently to the fracture toughness, as it provides a measure of the number of soft defects embedded inside glassy structures.^{14,15,29,30} Another measure of mesoscopic mechanical disorder in glasses can be defined using the fluctuations of the shear modulus μ .^{29,37–40} This measure, denoted hereafter by χ (see “Materials and methods” section and Figure 1h), has been recently shown to control the rate of wave attenuation in computer glasses,^{39,41,42} (i.e., the amplitude of Rayleigh scattering rates in the low-frequency [long-wavelength] limit). In this article, we will be using A_g and χ as quantifiers of mesoscopic glassy disorder, which are directly relevant to the fracture toughness.

A_g and χ allow one to compare on equal footing different glasses, either glasses of the same interatomic interactions/composition formed by different thermal protocols or glasses of different interatomic interactions/composition. While existing evidence clearly indicates that A_g and χ must play important roles in determining the fracture toughness of these materials, one obviously cannot exclude the possibility that other physical quantities and factors play a role as well. Indeed, some experimental and computational studies^{4–6,43–46} suggested that Poisson’s ratio ν plays an important role in determining the fracture toughness of glasses (though some other studies challenged this view).^{7,29,47} A possible interpretation is that ν is sensitive to the structure of a glass, and in particular, that it may be indirectly related to plastic deformability and its sensitivity to shear versus tensile deformation,^{6,48} and hence affects the toughness. As such, one can speculate that the observed effect of ν is not qualitatively different from that of A_g and χ —indeed we show below that well-defined relations between ν and A_g (and χ) exist. It remains unclear, however, whether ν —or more precisely Poisson contraction/effect and other loading geometry effects—also play distinct roles in determining the toughness.

Our goal in this article is to understand the roles played by soft defects, as quantified by A_g and indirectly by χ , and by the loading geometry employed in mechanical tests on the fracture toughness of glasses, in particular on brittle-to-ductile transitions. This goal is achieved by employing extensive computer glass simulations in 3D, which offer a powerful and flexible platform to address the posed questions. To mimic

glasses’ compositional variability, we employ computer models based on Lennard–Jones interatomic pairwise potentials with a *tunable* parameter r_c (to be accurately defined next), shown recently to give rise to glasses of widely variable properties.^{29,49–51} We also apply a broad range of cooling rates \dot{T} across the glass transition (to be accurately defined next). In addition, we employ cutting-edge algorithms that allow to generate deeply supercooled glasses,⁴⁰ to a degree that is comparable or even surpasses that of laboratory glasses. Overall, the range of variability of the macroscopic properties (e.g., μ and ν , Figure 1c–d) of our computer glasses is comparable to that observed in laboratory glasses. Finally, we carefully and systematically vary the imposed loading geometry in the fracture toughness tests in order to quantify its effect on the toughness.

We find that the fracture toughness, and in particular brittle-to-ductile transitions, are controlled by *both* the abundance of soft defects—as quantified by A_g (and indirectly by χ)—and by the loading geometry of the fracture test. The latter affects the relative magnitude of shear and tensile deformation experienced by the material, and consequently the emerging plastic dissipation, for a fixed A_g . That is, the loading geometry controls the activation of soft defects, whose abundance is controlled by A_g . Only under a certain choice of loading geometry, where Poisson contraction can take place, Poisson’s ratio ν can be sensibly used to quantify the fracture toughness *together* with A_g (or χ). These results provide basic insights into the physical origin of the failure resistance of glasses.

Results

In order to study the origin of brittle-to-ductile transitions in glasses, such as the one illustrated in Figure 1a, we first aim at generating computer glasses featuring a broad range of properties. This is achieved by employing the computer glass model put forward in Reference 49, where particles interact via a tunable Lennard–Jones-like pairwise potential (a similar approach was taken in Reference 52). In particular, the strength and range of the attractive term of the pairwise potential are controlled by a parameter r_c , as shown in Figure 1b and accurately defined in “Materials and methods” section. Varying r_c , which may qualitatively correspond to varying the glass composition, results in dramatic changes in emergent material properties, as will be discussed and demonstrated soon (see also References 29 and 50). In addition, we generate different glasses by quenching equilibrium liquids at a broad range of rates into their arrested glass phase. The cooling rate is quantified by \dot{T} , the dimensionless absolute value of the rate of change of temperature during the quench (see “Materials and methods” section for precise definition). Yet another glass formation protocol, which is not quantified by \dot{T} , is employed and discussed next.

In Figure 1c, we present the shear modulus μ (in simulation units, see “Materials and methods” section) as a function of \dot{T} for various values of r_c . The corresponding results for



Poisson's ratio ν are shown in Figure 1d. The range of variation in ν accessed by tuning r_c compares well with the one for which the so-called ductile-to-brittle transition is observed in bulk metallic glasses,⁵³ and see *Supplementary Information* for further comparisons between our model's elastic properties and typical laboratory glasses' elastic properties. While our model's macroscopic linear response coefficients make direct contact with laboratory glasses, computer glasses offer unique access to various physical quantities that are not directly accessible to experiments, as previously highlighted. In Figure 1e, we present the vDOS of QLMs for two values of r_c and a fixed \dot{T} , both revealing the universal $\mathcal{D}(\omega) = A_g \omega^4$ law. Here and elsewhere, we report frequencies in terms of $\omega_0 \equiv c_s/a_0$, where c_s is the (zero frequency) shear wave speed and $a_0 \equiv (V/N)^{1/3}$ (V is the system's volume containing N particles). The observed prefactor A_g vastly varies between the two cases. A_g , made dimensionless through multiplication by ω_0^5 , is presented in Figure 1f for all \dot{T} and r_c values used in Figure 1c–d. The dimensionless A_g (hereafter we exclusively refer to the dimensionless one) indeed reveals large variability (notice the logarithmic scale in Figure 1f). Interestingly, different combinations of \dot{T} and r_c result in nearly identical A_g values (marked by open orange squares), a property that will be used next.

A_g , providing a measure of the abundance of soft defects inside a glass,¹⁵ serves as a disorder quantifier that is relevant for plastic deformability and fracture toughness. Another quantifier of mechanical disorder in glasses can be obtained by considering

the distribution of the local shear modulus, probed by studying a large number of systems of size N .^{39,51} In Figure 1g, we present the shear modulus distributions corresponding to the two cases shown in Figure 1e. It is observed that smaller A_g glasses feature reduced shear modulus fluctuations $\Delta\mu/\mu$. The latter can be used to construct an N -independent quantifier of mechanical disorder in the form $\chi \equiv (\Delta\mu/\mu)\sqrt{N}$.^{39,41,42,51} The dependence of χ on both r_c and \dot{T} is presented in Figure 1h, and the relation between χ and A_g is further discussed next (Figure 3d and *Supplementary Information*). Next, we start considering the fracture toughness of the glasses at hand.

Reduction in cooling rate can induce a ductile-to-brittle transition

In order to probe the fracture toughness, we consider 3D glass samples containing an initial central crack of fixed geometry that cuts through the sample (in the thickness direction). In particular, we choose a diamond-shaped crack of fixed length and main vertex angle, which give rise to traction-free crack surfaces. The main vertex angle is chosen to be sufficiently small in order to reproduce the classical square root singularity of linear elastic fracture mechanics,² see *Supplementary Information* for additional details. The initial crack length is chosen to be sufficiently larger than the particle size and sufficiently smaller than the sample's dimensions in order to ensure reasonable scale separation, though we cannot entirely exclude any finite size effects (see *Supplementary Information*). All fracture toughness calculations are performed under quasistatic athermal conditions (i.e., vanishing applied strain-rate and zero temperature), as our focus is on the effect of glass structure and loading geometry on the toughness.

We first consider the effect of varying the cooling rate \dot{T} on the glass resistance to failure under unconstrained uniaxial tension, where 'unconstrained' means that the lateral edges (perpendicular to the tensile axis) are traction-free and hence free to contract. We focus here on the $r_c = 1.3$ glass ensemble, and plot in Figure 2a the tensile stress–strain curves for four different cooling rates \dot{T} (see legend). It is observed that for the two largest \dot{T} values, the corresponding glasses feature gradual stress relaxation after reaching a peak stress, with no clear sign of catastrophic failure. For the two smallest \dot{T} values, however, the glass appears to lose its load-bearing capacity at a well-defined strain level, indicating catastrophic failure.

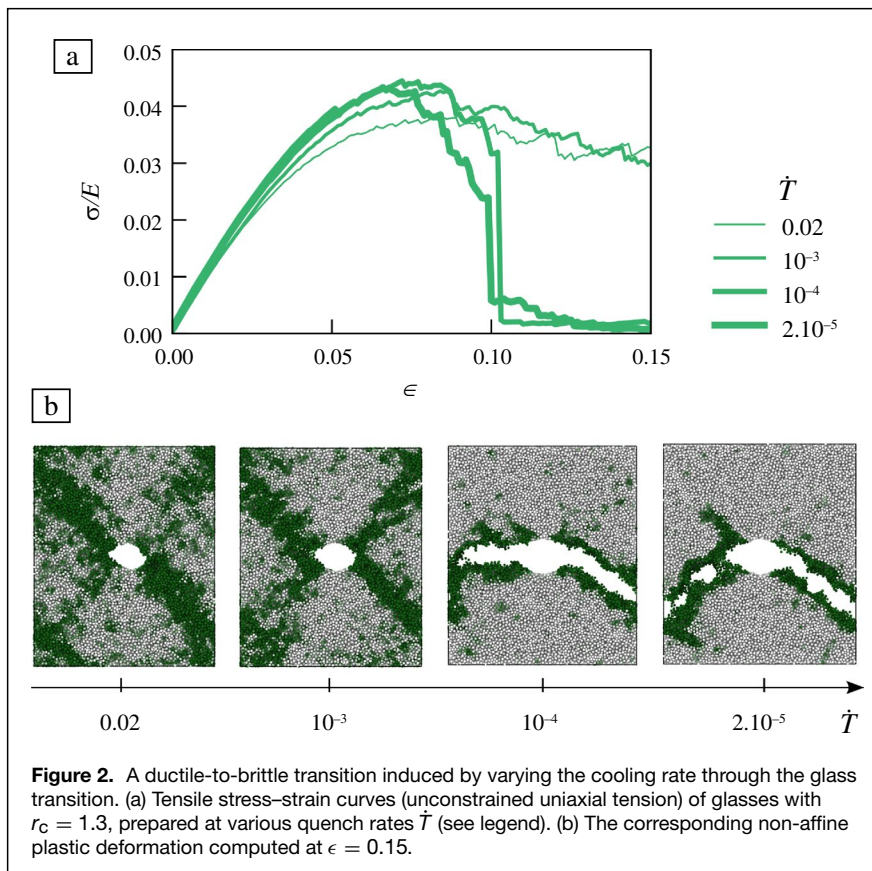


Figure 2. A ductile-to-brittle transition induced by varying the cooling rate through the glass transition. (a) Tensile stress–strain curves (unconstrained uniaxial tension) of glasses with $r_c = 1.3$, prepared at various quench rates \dot{T} (see legend). (b) The corresponding non-affine plastic deformation computed at $\epsilon = 0.15$.

Consequently, there appears to exist a cooling rate that induces a ductile-to-brittle transition, as was also demonstrated in the previous work.^{9,54–56} This is corroborated by the spatiotemporal dynamics of the deformed samples, as demonstrated in Figure 2b, where snapshots at 15% strain are shown. Consistent with the stress–strain curves, we observe that while glasses formed under the two highest cooling rates feature a blunted crack accompanied by large-scale plastic deformation (darker regions, see figure caption), glasses cooled at the two lowest rates feature a crack that propagates through the samples, accompanied by rather localized plastic deformation.

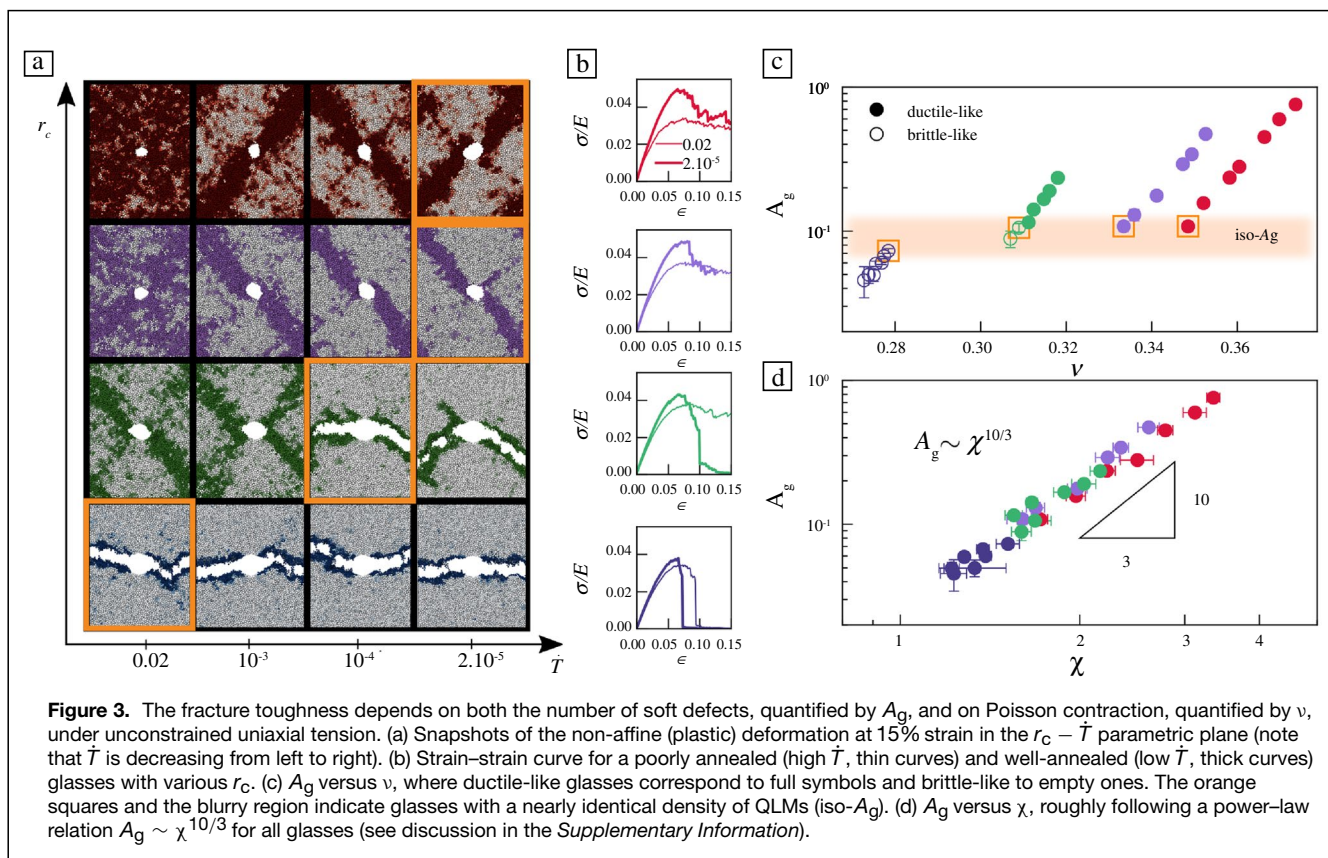
It is known that varying the cooling rate \dot{T} leads to varying glass structures and consequently to variation in many material properties of a glass.^{14,57,58} Our next goal is to understand which physical properties control the ductile-to-brittle transition observed in Figure 2, when \dot{T} is varied.

Do soft defects exclusively control the ductile-to-brittle transition? The role of Poisson contraction under unconstrained uniaxial tension

As explained in the Introduction, A_g —whose \dot{T} dependence is presented in Figure 1f—is a natural candidate for controlling the observed ductile-to-brittle transition. To test this natural expectation, we cannot restrict ourselves to a single r_c value; rather, we employ glasses cooled at different quench rates \dot{T} and of different interaction parameters r_c that nevertheless share nearly the *same* (dimensionless) A_g . These glasses, which are marked by open orange squares in Figure 1f, are expected to

feature similar resistance to failure—if indeed A_g fully controls the fracture toughness of glasses. In Figure 3a, we plot 15% strain snapshots in the $r_c - \dot{T}$ parametric plane (covering the whole range of employed parameters)—similarly to Figure 2b (in fact, the latter is reproduced here in the third row from the top)—, where the nearly iso- A_g are highlighted by open orange rectangles. It is observed that iso- A_g glasses are either brittle-like or ductile-like, indicating that A_g does not exclusively control the fracture toughness under the present conditions (i.e., under unconstrained uniaxial tension). This conclusion is corroborated by the stress–strain curves presented in Figure 3b. In addition, it is observed that ductile-like behavior (e.g., the top two rows of Figure 3a) is accompanied by the formation of shear bands, whose width appears to decrease with decreasing \dot{T} . We hypothesize that this trend might echo recent results demonstrating that the typical linear size of soft defects/STZs decreases by up to a factor of two upon thermal annealing.¹⁵

What additional physical quantities/factors/processes, which also vary with \dot{T} , play a role in ductile-to-brittle transitions in glasses? These, once identified, should allow to differentiate between the qualitatively different behaviors observed among the iso- A_g glasses, highlighted by open orange rectangles in Figure 3a. As explained in the Introduction, there exists some evidence^{4–6,43–46} that Poisson’s ratio ν might affect the fracture toughness of glasses. The \dot{T} dependence of ν for our glasses is presented in Figure 1d, clearly indicating that iso- A_g glasses feature different ν ’s (marked by open orange squares). Consequently, we present in Figure 3c a brittle–ductile phase



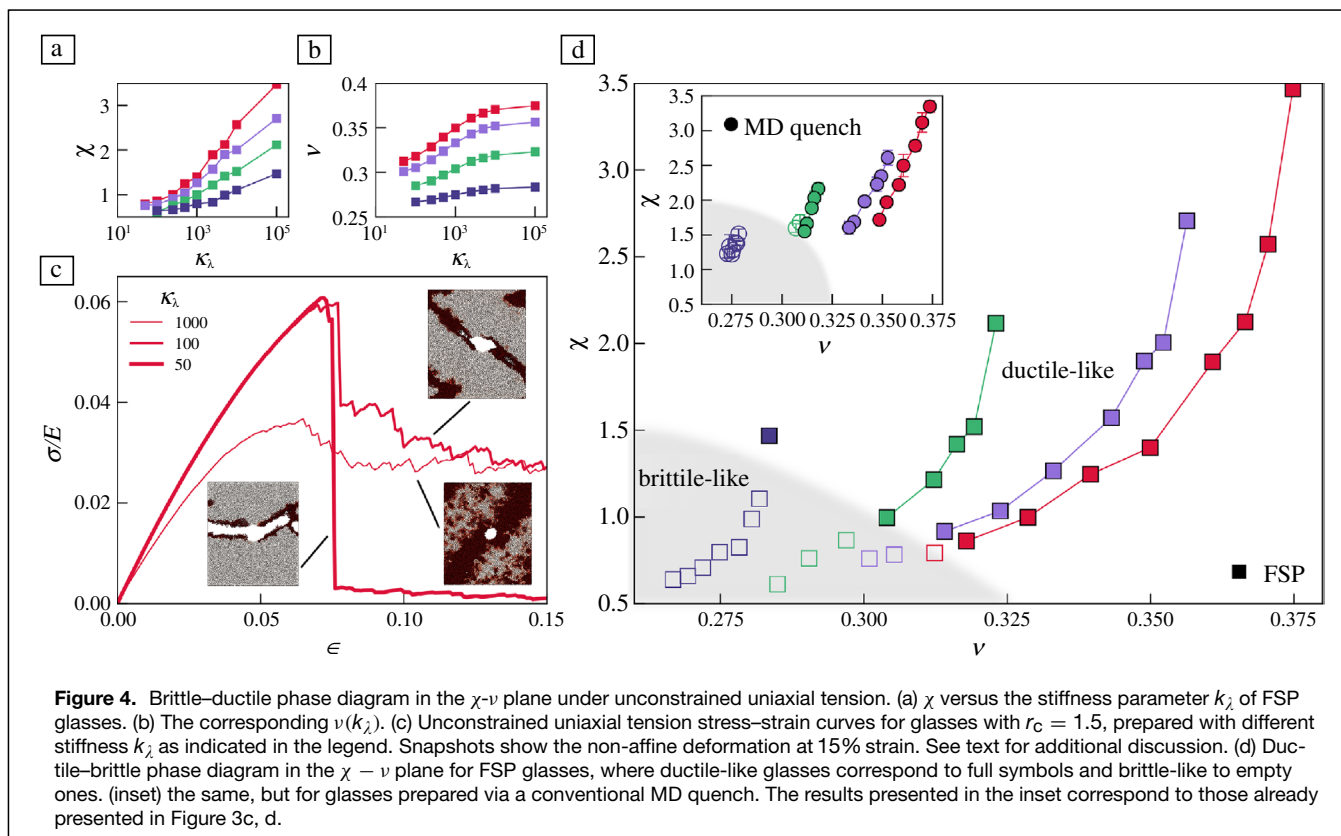


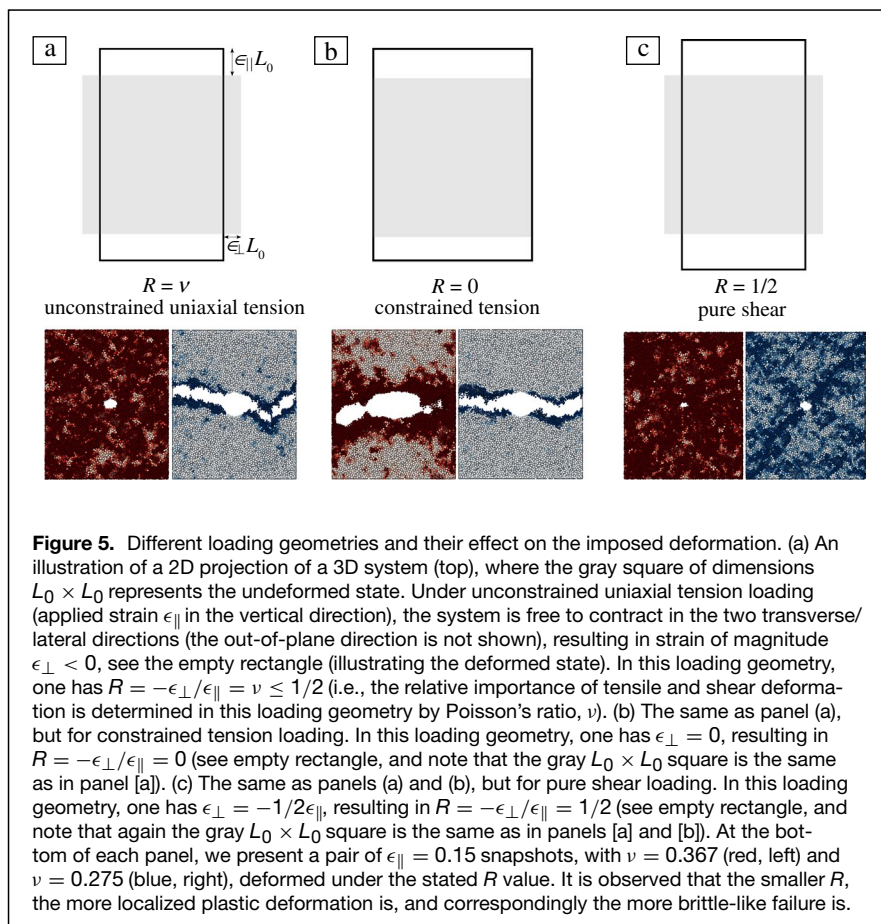
diagram in the A_g – ν plane, where ductile-like glasses correspond to full symbols and brittle-like to empty ones (we include data for all of our glasses, across the full range of \dot{T} and r_c values employed, as in Figure 1). It is observed that iso- A_g glasses of relatively high ν are ductile-like, while those with smaller ν are brittle-like. This indicates that ν might indeed play a role in the fracture toughness of glasses.

What is the physical (and causal) effect of ν on the fracture toughness? Before setting out to address this important question, we aim at further substantiating the claim that both glassy disorder—as quantified by either A_g or χ —and some effect that is related to ν play a role in determining the fracture toughness of glasses. The results presented in Figure 3c clearly support this claim, yet for relatively large values of r_c it is impossible to reach sufficiently small A_g levels to probe the brittle regime using conventional Molecular Dynamics (in which glasses are formed by quenching their corresponding liquids). Consequently, we employ next recently introduced computer algorithms that allow the generation of glassy solids featuring $A_g \rightarrow 0$, qualitatively representing extreme supercooling conditions.

To this aim, we first note that as shown in Figure 3d, glasses form by quenching a liquid feature a clear relation between A_g and χ (see also *Supplementary Information*). The existence of such a relation, which appears to be weakly dependent on r_c , suggests that for these glasses one can approximately use A_g and χ interchangeably. This is not the case for systems featuring $A_g \rightarrow 0$. The latter can be generated by a protocol that is

referred to in what follows as the *FSP algorithm*, described in detail in “[Materials and methods](#)” section and in Reference 40; forming a computer glass using the FSP algorithm amounts to minimizing an augmented potential parameterized by a stiffness k_λ that controls the mechanical noise of the resulting glasses (while r_c can still be varied, see “[Materials and methods](#)” section), with lower- k_λ FSP glasses featuring less mechanical fluctuations.⁴⁰ As is now established, FSP glasses can feature a gap in their non-phononic vDOS⁴⁰ for sufficiently small k_λ , and in particular in this limit they do not feature the ω^4 law. That is, lower- k_λ FSP glasses essentially feature $A_g \rightarrow 0$. Yet, these glassy solids still exhibit a finite and well-defined χ , as demonstrated in Figure 4a. Moreover, ν also varies systematically with k_λ and r_c , as shown in Figure 4b.

The merit of FSP glasses in the present context is evident from panels (a) and (b) of Figure 4. That is, we have at hand glasses with $A_g \rightarrow 0$ (in the low k_λ regime), whose χ and ν can be systematically varied. Consequently, FSP glasses are most suitable for exploring the ductile-to-brittle transition in terms of both χ and ν , providing access to broader region of the brittle-like phase. In Figure 4c, we present the stress–strain curves of FSP glasses with $r_c = 1.5$ for three values of k_λ , together with spatial snapshots of each glass at a late stage in the loading process. For the largest k_λ value ($k_\lambda = 1000$), the behavior is ductile-like, exhibiting extensive (system covering) plastic deformation and steady-state flow, essentially being insensitive to the initial crack. For the smallest k_λ value ($k_\lambda = 50$), we enter into



the brittle-like regime, where catastrophic failure takes place, accompanied by localized plastic deformation near the crack (which is predominantly perpendicular to the tensile axis) and an abrupt drop in the stress when the sample loses its load-bearing capacity. Interestingly, for the intermediate k_{λ} value ($k_{\lambda} = 100$), the initial crack started growing along an inclined shear-band (resulting in a finite abrupt stress drop), but eventually plastic deformation in the shear-band took over (resulting in a gradual stress relaxation towards a plateau), with no catastrophic failure.

We performed an extensive analysis of all FSP glasses at hand (the four r_c values studied earlier and a broad range of k_{λ} values) and present the results in Figure 4d in a phase diagram in the χ - ν plane, where a ductile-like behavior corresponds to full squares (color code as in Figure 1) and a brittle-like behavior corresponds to empty squares. First, it is observed that indeed FSP glasses allow to explore a broader region of the brittle-like phase. Second, and most importantly, it is observed that both χ and ν (more precisely some effect that is related to ν) play a role in the ductile-to-brittle transition, as is evident from the curved phase boundary (a blurry region is added as a guide to the eye).

Finally, we add in the inset the results for the glasses formed by quenching a liquid—presented earlier in Figure 3 (but not in the χ - ν plane). Interestingly, despite the widely different glass formation protocols involved, the two classes of glasses appear

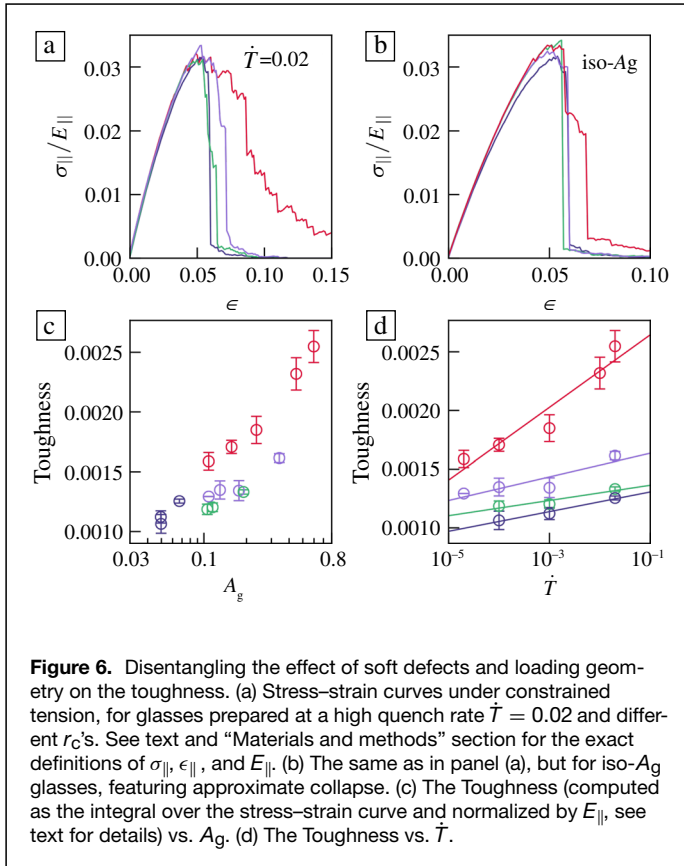
to reveal a qualitatively similar ductile–brittle phase diagram in the χ - ν plane, where both decreasing χ and ν promote a brittle-like behavior. It is important to note again that the results presented in Figure 4d were obtained for our choice of initial crack of fixed geometry and dimensions (see also *Supplementary Information*); varying the latter may change quantitative aspects of the results, but the combined effect of χ and ν on the fracture toughness under unconstrained uniaxial tension conditions is general. Once this is established, we focus our attention on the question previously posed regarding the physical (and causal) effect of ν on the fracture toughness, which is addressed next.

The interplay of loading geometry and plastic deformability: Constrained tension and soft defects again

Poisson's ratio ν is a linear elastic (reversible) response coefficient that quantifies the relative transverse contraction of a material under unconstrained (transversely free) uniaxial tension. In assessing

the relevance of ν to the fracture toughness of glasses, one can a priori distinguish two qualitatively different classes of physical effects. First, ν can be viewed as a directly and easily measurable quantity that allows to indirectly probe non-linear irreversible response coefficients that are relevant for plastic deformability and toughness. Indeed, ν is expected to vary when the material structure and interactions vary, and in particular it exhibits systematic variations with A_g and χ , as demonstrated in Figures 3 and 4. Second, ν —as a linear elastic coefficient—may affect the geometry of deformation glasses experience under external driving forces. In particular, in the unconstrained uniaxial tension tests exclusively considered up to now, ν controls the degree of Poisson contraction, which in turn determines the relative magnitude of tensile and shear deformation. That is, ν in this loading geometry will affect the activation of soft defects (whose number is controlled by A_g), which are generally more sensitive to shear deformation.

As physically relevant disorder measures such as A_g and χ have been identified and quantified, we hypothesize that a linear elastic response coefficient such as ν does not contain *additional* physical information about plastic deformability, on top of A_g and/or χ . Consequently, while in the absence of well-founded quantifiers of glassy disorder one may use ν as some



rough proxy of disorder, when these are at hand and taken into account—as is the case here—the effect of ν in the phase diagram of Figure 4d strongly points towards the second possibility previously discussed. That is, one needs to understand the role of the deformation/loading geometry on the fracture toughness, both in relation to ν and in more general terms.

To address the latter, we introduce here the biaxiality ratio R (Figure 5), defined as $R \equiv -\epsilon_{\perp}/\epsilon_{\parallel}$, where ϵ_{\parallel} is the tensile/extensional strain and ϵ_{\perp} corresponds to the transverse strains (i.e., the strain components in the directions perpendicular to the applied tension axis). The main utility of R is that it quantifies the relative importance of tensile and shear deformation imposed by the loading geometry, and since soft defects (STZs) are most sensitive to shear deformation,³ R offers a simple measure of the fraction of soft defects being activated under a certain loading geometry (while their number is controlled by A_g). Since, in principle, ϵ_{\parallel} and ϵ_{\perp} can be independently controlled, R can take any value (and can even evolve during a mechanical test). Yet, we focus here on a few cases that are most relevant to our discussion. For pure shear deformation, defined by the absence of linear dilatational strain ($\epsilon_{\parallel} + 2\epsilon_{\perp} = 0$), we have $R = 1/2$. As plastic deformation in glasses is most sensitive to shearing,³ this value of R is expected to facilitate a more plastic response, see Figure 5c. For the unconstrained uniaxial tension loading geometry considered up to now, we have $R = \nu \leq 1/2$; that is, R in this loading geometry is determined by a material property, quantified

by ν . Therefore, we see that reducing ν in the unconstrained loading configuration tends to increase the relative importance of tensile deformation (Figure 5a), which may facilitate a more brittle-like behavior, in qualitative agreement with the results of Figure 4d.

As R is in general not a material property, but can rather be controlled through the imposed loading geometry, one can use it to disentangle the roles of A_g (or χ) (i.e., the role of soft defects) and of the loading geometry on the fracture toughness. To that aim, we performed constrained tension tests, where the transverse/lateral boundaries (perpendicular to the main tensile axis) are held fixed (i.e., $\epsilon_{\perp} = 0$). This case corresponds to $R = 0$, see Figure 5b and “Materials and methods” section for additional discussion. The loading geometry corresponding to $R = 0$ allows to eliminate the role of ν as a linear response coefficient that controls Poisson contraction. Consequently, we expect the fracture toughness in this case to be determined by A_g . Since for $R = 0$, which obviously favors tensile deformation, catastrophic failure is unavoidable, A_g is expected to affect the value of the fracture toughness, not strictly a brittle-to-ductile transition. In particular, we expect iso- A_g glasses to feature very similar toughness under constrained tension, despite having different ν 's, and the toughness to systematically increase with A_g for the same glass cooled at different rates \dot{T} .

These predictions are tested in Figure 6, where we first show in panel (a) that different glasses (i.e., different r_c values) feature rather large variability in their failure behavior under constrained tension for a fixed cooling rate \dot{T} (here we present stress–strain curves; a quantitative measure of the fracture resistance is presented in panels [c] and [d]). The discussion above predicts that if one repeats the calculations of Figure 6a for different glasses featuring nearly the same A_g , under the same constrained tension loading geometry ($R = 0$), most of the variability in the failure behavior would be gone. The results of these calculations are presented in Figure 6b, where it is indeed observed that the stress–strain curves of iso- A_g glasses featuring different ν values, approximately collapse, as predicted. These results should be compared to—and contrasted with—the results shown in Figure 3c obtained under unconstrained uniaxial tension. We stress that these results strongly suggest that once the geometrical Poisson contraction is eliminated (or more generally when R is prescribed), Poisson's ratio ν does not play a major role in determining the toughness of glasses.

Another prediction discussed above is that the fracture toughness is expected to systematically increase with A_g under constrained tension. In order to test this prediction, we quantify the fracture resistance through the “Toughness,”⁵⁹ which is defined as the integral under the stress–strain curve up to failure (it has the dimensions of energy density, and should be distinguished from the “Fracture toughness” K_{Ic} ,² which has the dimensions of stress times the square root of length,



see *Supplementary Information*). Note that the Toughness is usually employed for samples that do not contain an initial crack (as it obviously depends on the crack geometry and dimensions); here we do apply it to such samples, but as done throughout this work, the initial crack geometry and dimensions are strictly kept fixed (in the *Supplementary Information* we discuss the effect of varying the initial crack length, as well as of varying the system thickness). In Figure 6c, we plot the Toughness versus A_g for our entire glass ensemble, calculated under constrained tension. As predicted, we observe systematic increase of the Toughness with A_g . Finally, we expect that the \dot{T} dependence of A_g , previously presented in Figure 1f, is fully and transparently mirrored in the dependence of the Toughness on \dot{T} . This is strongly supported by the results shown in Figure 6d.

Discussion and conclusion

In this work, employing extensive atomistic simulations and recently developed concepts, we studied the physical origin of the failure resistance of glasses, and in particular the emerging brittle-to-ductile transitions. We showed that these are controlled by both the abundance of soft defects—as quantified by A_g , the prefactor of the universal ω^4 vDOS of non-phononic excitations in glasses (and indirectly by χ)—and by the loading geometry of the fracture test employed to extract the toughness. The loading geometry/configuration is shown to affect the relative magnitude of shear and tensile deformation experienced by the material near the initial crack, and consequently the emerging plastic dissipation, for a fixed A_g . Roughly speaking, A_g controls the number of soft defects/STZs in a glass, and the loading geometry controls the fraction of soft defects/STZs being actually activated, and hence both affect plastic deformation and consequently the fracture toughness.

We find that only under a certain choice of loading geometry, where Poisson contraction can take place, Poisson's ratio ν can be sensibly used to quantify the fracture toughness together with A_g (or χ). These results suggest that brittle-to-ductile transitions in glasses are not controlled by a critical Poisson's ratio, as previously proposed, and elucidate the physical role ν might play in affecting the fracture toughness of glasses.

It is important to note that our results also show that while varying the interatomic potential, in our case using the parameter r_c as shown in Figure 1b, affects the fracture toughness, there exists no simple and direct relation between the particle-scale force–separation relation and the fracture toughness. In particular, one cannot read off the variation of the fracture toughness from just an isolated bond breaking process that is indicated by the interatomic potential. This is clearly demonstrated by Figure 6b, which shows that glasses with quite significantly different ranges of interatomic potentials fail in a similar manner if their A_g is similar. That is, our results indicate that the fracture toughness is a collective, emergent property of glasses, which depends on the non-equilibrium self-organization of a glass during its formation.

Our findings thus provide basic insights into the physical origin of the failure resistance of glasses, and should serve as important input for theories that aim at predicting it. Such theories should include the number of soft defects, as quantified here by A_g , and its deformation-induced spatiotemporal evolution as important ingredients. Our findings also call for additional future investigations, along the lines we delineate next.

In this work, we employed an athermal ($T = 0$) and quasistatic (i.e., we approach the limit of vanishing deformation rates) glass-deformation protocol.^{31,60} While this choice is suitable for identifying structural and loading geometry effects on the fracture toughness, it completely suppresses thermal and rate effects, and might therefore introduce uncontrolled artifacts. It is obviously desirable to extend the present study to more physically realistic loading protocols that involve both finite temperatures and strain rates.

Equally important for future work are mechanical tests on computer glasses that trace out the role of sample size and thickness in determining the failure resistance to failure; in this work we employed glassy slabs of small thickness (see “Materials and methods” section), hence systematically studying possible thickness effects is in place. In the *Supplementary Information*, we show that increasing the glass in-plane dimensions—other than the slab thickness—does not appear to affect the fracture behavior. In addition, as our results were obtained for an initial crack of fixed geometry and dimensions (but see also *Supplementary Information*), it would be important in future work to sufficiently increase both the system size and the initial crack size to obtain quantitative results that are entirely independent of both.

We selected to study a rather flexible computer glass model system—introduced first in Reference 49—that features a very large variability of glasses' mechanical properties.^{29,50} While we are unable at this point to single out a particular deficiency of this model, the employed pairwise interactions might be too simple to capture the emergent effects of more complex and realistic particle interactions of laboratory glasses in their entirety. For example, the Poisson ratio of our computer glasses does not fall below $\nu = 1/4$, while other (network) computer glasses (e.g., those employed in Reference 6) can feature $\nu < 1/4$. More generally, it would be important to extend the present study to more realistic interatomic interaction potentials (e.g., that include covalent interactions) and to multi-component glasses.

At the same time, the power of computer simulations allows us to probe and measure generally applicable quantifiers of mechanical disorder such as A_g and χ ; while the former does not appear to be directly accessible experimentally, the latter could be—in principle—indirectly accessed in future experiments via transverse sound attenuation measurements at wavenumbers $\lesssim \ln m^{-1}$, or via other experimental techniques.^{61,62} As new and more informative quantifiers of STZ densities are being developed (e.g., References 21, 36, and 63), we cannot rule out that more informative dimensionless



quantifiers of mechanical disorder can shed further light on the relation between mechanical disorder and plastic deformability, and hence on the fracture toughness.

In our analysis of the abundance of STZs as captured by A_g , we have not considered the effect of geometric/mechanical coupling of STZs to different deformation modes. In Reference 29 it was shown that varying r_c can dramatically affect the ratio of dilatational to shear eigenstrains associated with STZs viewed as Eshelby's inclusions. These changes in the intrinsic geometric properties of soft defects can potentially play a role in the failure of glasses. For example, the coupling of soft defects to different deformation modes can affect the susceptibility to cavitation, which is in fact observed in our simulations (but will be discussed elsewhere) as predicted in Reference 7.

Finally, our work constitutes a step toward a quantitative understanding of deformation-induced failure in disordered solids. Future investigations should aim at better understanding the role of deformation-induced rejuvenation of glassy structures—going beyond A_g that characterizes the *initial* glass structure—in controlling the ductile or brittle nature of failure. That is, plastic deformation itself could be limited—in some cases—in its ability to generate new soft defects that facilitate further plastic flow in the material, as typically happens within shear bands.⁶⁴

Materials and methods

Here, we provide details about the computer glass models employed, about the methods used to deform the glass samples, and about the observables considered.

Computer glass models

We employ a glass model put forward in Reference 49; in this model, particles of equal mass m interact via the following pairwise potential

where ε is a microscopic energy scale; x_{\min}, x_c are the (dimensionless) locations of the minimum of the Lennard–Jones potential and modified cutoff, respectively; and the λ_{ij} 's are the length parameters, described further next. We express the dimensionless cutoff x_c in terms of $x_{\min} = 2^{1/6}$, for simplicity, by defining $r_c \equiv x_c/x_{\min}$. r_c serves as one of the key control parameters in our study; we refer readers to References 29 and 50 for a comprehensive study of the *elastic* properties of glasses formed with this model, under variations of r_c and of glass preparation protocol. The coefficients $a, b, \{c_{2\ell}\}$ are chosen such that the attractive and repulsive parts of φ , and its first two derivatives, are continuous at x_{\min} and at x_c , see **Table I** for the coefficients' numerical values. Unless specified otherwise, we employ simulational units, where energies are expressed in terms of ε , temperature in terms of ε/k_B , lengths in terms of λ (see further discussion next), elastic moduli in terms of ε/λ^3 , and times in terms of $(m\lambda^2/\varepsilon)^{1/2}$.

We employ the pairwise potential in Equation (1) in two distinct protocols/procedures for creating glasses. For the first procedure, we follow the conventional computer glass formation route: high-temperature equilibrium liquid configurations at pressure $P = 1$ are generated at an initial temperature $T_{\text{initial}} = 0.7$. Those equilibrium configurations are then quenched at fixed zero pressure $P = 0$, and at a constant cool-

ing rate \dot{T} (as specified in the figure legends) until a temperature $T_{\text{final}} = 0.05$ is reached. Any residual heat is subsequently removed using a standard energy minimization algorithm. For this protocol, we employ a 50:50 binary mixture of 'large' (l) and 'small' (s) particles, and fix the effective size parameters $\lambda_{ss} = \lambda$, $\lambda_{sl} = \lambda_{ls} = 1.18\lambda$, and $\lambda_{ll} = 1.4\lambda$ for small–small, small–large, and large–large interactions, respectively.

Glasses formed with the second procedure—introduced next—are referred to as fluctuating-size-particles (FSP) glasses. They were created by employing the algorithm put forward in Reference 40; within this algorithm, an augmented

$$\varphi(r_{ij}, \lambda_{ij}) = \begin{cases} 4\varepsilon \left[\left(\frac{\lambda_{ij}}{r_{ij}}\right)^{12} - \left(\frac{\lambda_{ij}}{r_{ij}}\right)^6 \right], & \frac{r_{ij}}{\lambda_{ij}} < x_{\min} \\ \varepsilon \left[a \left(\frac{\lambda_{ij}}{r_{ij}}\right)^{12} - b \left(\frac{\lambda_{ij}}{r_{ij}}\right)^6 + \sum_{\ell=0}^3 c_{2\ell} \left(\frac{r_{ij}}{\lambda_{ij}}\right)^{2\ell} \right], & x_{\min} \leq \frac{r_{ij}}{\lambda_{ij}} < x_c \\ 0, & x_c \leq \frac{r_{ij}}{\lambda_{ij}} \end{cases} \quad (1)$$

Table I. Pairwise potential coefficients.

Coefficient	$r_c = 1.2$	$r_c = 1.3$	$r_c = 1.4$	$r_c = 1.5$
a	−106.991613526652	−17.7556513878655	−2.942014535960528	1.1582440286928275
b	−304.918469059567	−50.37332289908061	−12.11892507229410	−2.2619482444770567
c_0	−939.388037994211	−138.58271673010657	−35.72455291073821740	−12.414700446492716
c_2	1190.70962256002	161.71576064627635	38.70071979329345996	12.584354590303674
c_4	−541.3001315875512	−66.7252832098764	−14.5415594738601088	−4.320508006050397
c_6	85.86849369147127	9.50283097488097	1.86201465049568722	0.49862551162881885



potential energy is employed for creating glasses with very high variability of their mechanical stability. This variability is achieved during glass formation by allowing particle sizes λ_i to fluctuate about a preferred effective size $\lambda_i^{(0)}$ at an energetic penalty determined by a potential of the form

$$\tilde{\varphi}(\lambda_i) = \frac{k_\lambda}{2} (\lambda_i - \lambda_i^{(0)})^2 \left[\left(\frac{\lambda_i^{(0)}}{\lambda_i} \right)^2 + \frac{1}{4} \right], \quad (2)$$

where the stiffness k_λ constitutes the main control parameter of FSP glasses. Notice that this form is slightly different from the effective size potential used in Reference 40; the latter turns out to be unstable for small k_λ and small confining pressures. We set the preferred sizes of half the particles at $\lambda_i^{(0)} = \tilde{\lambda}/2$ (as before $\tilde{\lambda}$, forms the microscopic units of length), the other half at $\lambda_i^{(0)} = 7\tilde{\lambda}/10$, and used the convention $\lambda_{ij} = \lambda_i + \lambda_j$. Crucially, once a glass is created with the FSP algorithm, all subsequent analyses and mechanical tests are performed under *fixed* particle sizes λ_i , namely using the exact same pairwise potential as given by Equation (1). Importantly, local minima (glassy states in mechanical equilibrium) of the augmented potential also constitute local minima of the potential given by Equation (1). Finally, we note that the particles of FSP glasses are polydispersed in size, since during glass formation the effective particle sizes fluctuate, see Reference 40 for further discussion and details. We employ the FSP algorithm to create zero pressure glasses, starting from high-temperature liquid states and minimizing the augmented potential using a variety of stiffnesses k_λ (and various values of r_c) as reported in the figure legends. In general, decreasing the stiffness parameter k_λ results in stiffer glasses featuring less mechanical fluctuations.

Using the two procedures/protocols previously described, we created two sets of ensembles: one set was created for extracting the micromechanical properties of each ensemble as reported in Figure 1 for glasses formed with a finite cooling rate, and in Figure 4 for glasses formed using the FSP protocol. For these calculations, we prepared between 256 and 5000 glasses of $N = 4096$ particles (except for lowest cooling rate $\dot{T} = 2 \times 10^{-5}$ for which $N = 2197$). The second set of ensembles—prepared for our mechanical tests—were larger, rectangular glass slabs of dimensions $L_x \times L_y \times L_z$, with $L_x = L_y = L_0 = 60a_0$ and $L_z = 15a_0$ (recall that $a_0 \equiv (V/N)^{1/3}$), containing $N = 54,000$ particles in total.

Mechanical loading simulations

Mechanical loading is carried out via athermal quasistatic simulations, i.e., zero strain rate and temperature. For both unconstrained uniaxial tension and constrained tension (see also Figure 5 and “Mechanical and structural observables” next), the glass is affinely deformed by imposing an extensional strain along the y -axis (regarded as the parallel direction in the text). We define the extensional strain as $\epsilon_{\parallel} = (L - L_0)/L_0$, where L and L_0 are the current and initial box length along

\mathbf{e}_y , respectively. Particle positions are changed according to $y_i \rightarrow y_i + \delta\epsilon_{\parallel} y_i$, where the strain step $\delta\epsilon_{\parallel}$ is fixed at each step such that the accumulated extensional strain ϵ_{\parallel} increases by 10^{-3} . Subsequently, we minimize the potential energy U , where periodic boundary conditions are applied in all directions. For constrained tension, we employ the conventional conjugate gradient algorithm. For unconstrained uniaxial tension, we combine the FIRE minimization algorithm⁶⁵ with the Berendsen barostat. The latter keeps the stress in the transverse directions (i.e., along the x - and z -axis, zero, with a time constant $\tau_{\text{Ber}} = 10.0$). For both loading geometries, the minimization is stopped once the ratio between the typical gradient of the potential and the typical interparticle force drops below 10^{-10} . During each simulations, and closely following Reference 3, we monitor the non-affine part of the plastic deformation based on the commonly used D_{min}^2 field³ between the initial configuration ($\epsilon_{\parallel} = 0$) and the current state.

Mechanical and structural observables

The potential energy of our glasses is given by $U = \sum_{i < j} \varphi_{ij}(r_{ij})$, where the pairwise potential we employed is described in Equation (1). As we focus on athermal conditions, the shear modulus is defined as⁶⁶

$$\mu \equiv \frac{1}{V} \left(\frac{\partial^2 U}{\partial \gamma^2} - \frac{\partial^2 U}{\partial \gamma \partial \mathbf{x}} \cdot \mathcal{H}^{-1} \cdot \frac{\partial^2 U}{\partial \mathbf{x} \partial \gamma} \right), \quad (3)$$

where

$$\mathcal{H} \equiv \frac{\partial^2 U}{\partial \mathbf{x} \partial \mathbf{x}} \quad (4)$$

is the Hessian matrix of the potential U , and \mathbf{x} denotes particle coordinates. The latter are considered to transform via $\mathbf{x} \rightarrow \mathbf{H}(\gamma) \cdot \mathbf{x}$ with the parameterized shear transformation

$$\mathbf{H}(\gamma) = \begin{pmatrix} 1 & \gamma & 0 \\ 0 & 1 & 0 \\ 0 & 0 & 1 \end{pmatrix}. \quad (5)$$

The pressure is given by

$$p \equiv -\frac{1}{V \tilde{d}} \frac{\partial U}{\partial \eta}, \quad (6)$$

where $\tilde{d} = 3$ is the dimension of space, and η is the isotropic dilatational strain that parameterizes the suitable transformation of coordinates $\mathbf{x} \rightarrow \mathbf{H}(\eta) \cdot \mathbf{x}$ as

$$\mathbf{H}(\eta) = \begin{pmatrix} e^\eta & 0 & 0 \\ 0 & e^\eta & 0 \\ 0 & 0 & e^\eta \end{pmatrix}. \quad (7)$$

The athermal bulk modulus $K \equiv -\frac{1}{\tilde{d}} \frac{dp}{d\eta}$ is given by

$$K = \frac{1}{V \tilde{d}^2} \left(\frac{\partial^2 U}{\partial \eta^2} - \tilde{d} \frac{\partial U}{\partial \eta} - \frac{\partial^2 U}{\partial \eta \partial \mathbf{x}} \cdot \mathcal{H}^{-1} \cdot \frac{\partial^2 U}{\partial \mathbf{x} \partial \eta} \right). \quad (8)$$



With the definitions of the shear and bulk moduli in hand, the Poisson's ratio ν of a 3D solid is given by

$$\nu \equiv \frac{3K - 2\mu}{6K + 2\mu}. \quad (9)$$

As previously explained (see “Mechanical loading simulations” section) and in the main text, we employed two different types of loading geometries, namely unconstrained uniaxial tension and constrained tension (Figure 5). In the former, uniaxial tension of magnitude σ_{\parallel} is applied, while keeping the transverse stresses (in the two perpendicular directions) zero (i.e., $\sigma_{\perp} = 0$). The resulting extensional strain ϵ_{\parallel} satisfies $\sigma_{\parallel} = E\epsilon_{\parallel}$, where $E = 2\mu(1 + \nu)$ is the conventional Young's modulus. In this loading geometry, the biaxiality ratio is set by Poisson's ratio (i.e., $R = -\epsilon_{\perp}/\epsilon_{\parallel} = \nu$).

In the latter case, i.e., in the constrained tension loading configuration (Figure 5), the transverse boundaries (perpendicular to the applied tension direction) are held fixed (i.e., $\epsilon_{\perp} = 0$), and consequently the transverse stresses σ_{\perp} are no longer zero (in fact, they are tensile, for example, $\sigma_{\perp} > 0$). Note that since $\sigma_{\perp} \neq 0$ (i.e., the resulting state of stress is no longer uniaxial [though uniaxial stress $\sigma_{\parallel} > 0$ is applied], we term this loading geometry ‘constrained tension,’ omitting ‘uniaxial’). In this loading geometry, one can define two different moduli (linear response coefficients) E_{\parallel} and E_{\perp} , according to $\sigma_{\parallel} = E_{\parallel}\epsilon_{\parallel}$ and $\sigma_{\perp} = E_{\perp}\epsilon_{\perp}$. Using Hooke's Law, one finds

$$E_{\parallel} = 2\mu \frac{1 - \nu}{1 - 2\nu} \quad \text{and} \quad E_{\perp} = 2\mu \frac{\nu}{1 - 2\nu}. \quad (10)$$

These expressions are verified against numerical simulations in the *Supplementary Information*. Note that $E_{\parallel}(\mu, \nu) \geq E(\mu, \nu)$ for every μ and ν , and that in this case we have a zero biaxiality ratio (i.e., $R = -\epsilon_{\perp}/\epsilon_{\parallel} = 0$).

Quantifiers of mechanical disorder

In our work, we consider two dimensionless quantifiers of mechanical disorder. The first quantifier is defined as

$$\chi \equiv \frac{\Delta\mu}{\langle\mu\rangle} \sqrt{N}, \quad (11)$$

where $\Delta\mu$ is the ensemble-standard-deviation of the shear modulus μ (of glasses created with the exact same protocol), N is the system size, and $\langle\mu\rangle$ denotes the ensemble-average shear modulus. χ has been studied in Reference 29 under variations of glasses' interparticle interaction potential, and under different glass annealing protocols in References 39 and 51.

The second quantifier of mechanical disorder considered in our work is the prefactor A_g of the non-phononic spectrum of a glass, which is of the form $\mathcal{D}(\omega) = A_g\omega^4$, independent of spatial dimension²⁵ or microscopic details.²⁶ The latter is obtained by performing a partial diagonalization of the Hessian matrix \mathcal{H} , defined in Equation (4), and calculated

for each member of our glass ensembles, to obtain the eigenfrequencies ω_{ℓ} that solve the eigenvalue problem $\mathcal{H} \cdot \psi_{\ell} = \omega_{\ell}^2 \psi_{\ell}$ (all masses are all set to unity). We then histogram the eigenfrequencies for each glass ensemble, to obtain their distribution $\mathcal{D}(\omega)$ over the frequency axis. Importantly, we note that the scaling form of $\mathcal{D}(\omega) \sim \omega^4$ is most readily observable in glasses of sizes small enough to suppress the otherwise-dominant phononic waves that emerge in the low-frequency spectrum of any elastic solid, as explained in detail in Reference 19.

Acknowledgments

D.R. acknowledges support of the Simons Foundation for the “Cracking the Glass Problem Collaboration” Award No. 348126. E.L. acknowledges support from the NWO (Vidi Grant No. 680-47-554/3259). E.B. acknowledges support from the Ben May Center for Chemical Theory and Computation and the Harold Perlman Family.

Supplementary Information

The online version contains supplementary material available at <https://doi.org/10.1557/s43577-021-00171-8>.

References

1. J.S. Harmon, M.D. Demetriou, W.L. Johnson, M. Tao, *Appl. Phys. Lett.* **90**, 131912 (2007)
2. B. Lawn, *Fracture of Brittle Solids* (Cambridge University Press, Cambridge, 1993)
3. M.L. Falk, J.S. Langer, *Phys. Rev. E* **57**, 7192 (1998)
4. J.J. Lewandowski, W.H. Wang, A.L. Greer, *Philos. Mag. Lett.* **85**, 77 (2005)
5. S. Madge, D. Louzguine-Luzgin, J. Lewandowski, A. Greer, *Acta Mater.* **60**, 4800 (2012)
6. Y. Shi, J. Luo, F. Yuan, L. Huang, *J. Appl. Phys.* **115**, 043528 (2014)
7. C.H. Rycroft, E. Bouchbinder, *Phys. Rev. Lett.* **109**, 194301 (2012)
8. M. Vasoya, C.H. Rycroft, E. Bouchbinder, *Phys. Rev. Appl.* **6**, 024008 (2016)
9. J. Ketkaew, W. Chen, H. Wang, A. Datye, M. Fan, G. Pereira, U.D. Schwarz, Z. Liu, R. Yamada, W. Drmowski, M.D. Shattuck, C.S. O'Hern, T. Egami, E. Bouchbinder, J. Schroers, *Nat. Commun.* **9**, 3271 (2018)
10. J. Sethna, *Statistical Mechanics: Entropy, Order Parameters, and Complexity*, vol. 14 (Oxford University Press, Oxford, 2006)
11. D. Coslovich and G. Pastore, *J. Chem. Phys.* **127**, 124504 (2007)
12. H. Tong, H. Tanaka, *Phys. Rev. Lett.* **124**, 225501 (2020)
13. C.P. Royall, S.R. Williams, *Phys. Rep.* **560**, 1 (2015)
14. L. Wang, A. Ninarello, P. Guan, L. Berthier, G. Szamel, E. Flenner, *Nat. Commun.* **10**, 26 (2019)
15. C. Rainone, E. Bouchbinder, E. Lerner, *Proc. Natl Acad. Sci. U.S.A.* **117**, 5228 (2020)
16. B.B. Laird, H.R. Schober, *Phys. Rev. Lett.* **66**, 636 (1991)
17. H.R. Schober, C. Oligschleger, *Phys. Rev. B* **53**, 11469 (1996)
18. J. Ding, S. Patinet, M.L. Falk, Y. Cheng, E. Ma, *Proc. Natl Acad. Sci. U.S.A.* **111**, 14052 (2014)
19. E. Lerner, G. Düring, E. Bouchbinder, *Phys. Rev. Lett.* **117**, 035501 (2016)
20. H. Mizuno, H. Shiba, A. Ikeda, *Proc. Natl Acad. Sci. U.S.A.* **114**, E9767 (2017)
21. D. Richard, G. Kapteijns, J.A. Giannini, M.L. Manning, E. Lerner, *Phys. Rev. Lett.* **126**, 015501 (2021)
22. A. Moriel, Y. Lubomirsky, E. Lerner, E. Bouchbinder, *Phys. Rev. E* **102**, 033008 (2020)
23. V.L. Gurevich, D.A. Parshin, H.R. Schober, *Phys. Rev. B* **67**, 094203 (2003)
24. D.A. Parshin, H.R. Schober, V.L. Gurevich, *Phys. Rev. B* **76**, 064206 (2007)
25. G. Kapteijns, E. Bouchbinder, E. Lerner, *Phys. Rev. Lett.* **121**, 055501 (2018)
26. D. Richard, K. González-López, G. Kapteijns, R. Pater, T. Vaknin, E. Bouchbinder, E. Lerner, *Phys. Rev. Lett.* **125**, 085502 (2020)
27. C. Rainone, P. Urbani, F. Zamponi, E. Lerner, E. Bouchbinder, *SciPost Phys. Core* **4**, 008 (2021)
28. E. Bouchbinder, E. Lerner, C. Rainone, P. Urbani, F. Zamponi, *Phys. Rev. B* **103**, 174202 (2021)



29. K. González-López, M. Shivam, Y. Zheng, M.P. Ciamarra, E. Lerner, *Phys. Rev. E* **103**, 022605 (2021)
30. W. Ji, T.W.J. de Geus, M. Popović, E. Agoritsas, M. Wyart, *Phys. Rev. E* **102**, 062110 (2020)
31. C. Maloney, A. Lemaître, *Phys. Rev. Lett.* **93**, 195501 (2004)
32. A. Tanguy, B. Mantsi, M. Tsamados, *EPL* **90**, 16004 (2010)
33. M.L. Manning, A.J. Liu, *Phys. Rev. Lett.* **107**, 108302 (2011)
34. J. Rottler, S.S. Schoenholz, A.J. Liu, *Phys. Rev. E* **89**, 042304 (2014)
35. L. Gartner, E. Lerner, *Phys. Rev. E* **93**, 011001 (2016)
36. D. Richard, M. Ozawa, S. Patinet, E. Stanifer, B. Shang, S.A. Ridout, B. Xu, G. Zhang, P.K. Morse, J.-L. Barrat, L. Berthier, M.L. Falk, P. Guan, A.J. Liu, K. Martens, S. Sastry, D. Vandembroucq, E. Lerner, M.L. Manning, *Phys. Rev. Mater.* **4**, 113609 (2020)
37. M. Tsamados, A. Tanguy, C. Goldenberg, J.-L. Barrat, *Phys. Rev. E* **80**, 026112 (2009)
38. H. Mizuno, S. Mossa, J.-L. Barrat, *Phys. Rev. E* **87**, 042306 (2013)
39. G. Kapteijns, D. Richard, E. Bouchbinder, E. Lerner, *J. Chem. Phys.* **154**, 081101 (2021)
40. G. Kapteijns, W. Ji, C. Brito, M. Wyart, E. Lerner, *Phys. Rev. E* **99**, 012106 (2019)
41. W. Schirmacher, *Europhys. Lett.* **73**, 892 (2006)
42. W. Schirmacher, G. Ruocco, T. Scopigno, *Phys. Rev. Lett.* **98**, 025501 (2007)
43. J. Schroers, W.L. Johnson, *Phys. Rev. Lett.* **93**, 255506 (2004)
44. A. Castellero, S.D. Uhlenhaut, B. Moser, J.F. Löer, *Philos. Mag. Lett.* **87**, 383 (2007)
45. G.N. Greaves, A. Greer, R.S. Lakes, T. Rouxel, *Nat. Mater.* **10**, 823 (2011)
46. B. Deng, Y. Shi, *J. Appl. Phys.* **124**, 035101 (2018)
47. G. Kumar, P. Neibecker, Y.H. Liu, J. Schroers, *Nat. Commun.* **4**, 1 (2013)
48. Y.H. Liu, G. Wang, R.J. Wang, D.Q. Zhao, M.X. Pan, W.H. Wang, *Science* **315**, 1385 (2007)
49. O. Dauchot, S. Karmakar, I. Procaccia, J. Zylberg, *Phys. Rev. E* **84**, 046105 (2011)
50. K. González-López, M. Shivam, Y. Zheng, M.P. Ciamarra, E. Lerner, *Phys. Rev. E* **103**, 022606 (2021)
51. K. González-López, E. Bouchbinder, E. Lerner, arXiv preprint (2020). [arXiv:2012.03634](https://arxiv.org/abs/2012.03634)
52. M. Falk, *Phys. Rev. B* **60**, 7062 (1999)
53. D. Wang, D. Zhao, D. Ding, H. Bai, W. Wang, *J. Appl. Phys.* **115**, 123507 (2014)
54. F. Yuan, L. Huang, *J. Non-Cryst. Solids* **358**, 3481 (2012)
55. W. Li, Y. Gao, H. Bei, *Sci. Rep.* **5**, 1 (2015)
56. E.Y. Lin, R.A. Riggleman, *Soft Matter* **15**, 6589 (2019)
57. J. Ashwin, E. Bouchbinder, I. Procaccia, *Phys. Rev. E* **87**, 042310 (2013)
58. E. Lerner, E. Bouchbinder, *J. Chem. Phys.* **148**, 214502 (2018)
59. M.A. Meyers, K.K. Chawla, *Mechanical Behavior of Materials* (Cambridge University Press, Cambridge, 2008)
60. D.L. Malandro, D.J. Lacks, *J. Chem. Phys.* **110**, 4593 (1999)
61. L. Huo, J. Zeng, W. Wang, C.T. Liu, Y. Yang, *Acta Mater.* **61**, 4329 (2013)
62. F. Zhu, A. Hirata, P. Liu, S. Song, Y. Tian, J. Han, T. Fujita, M. Chen, *Phys. Rev. Lett.* **119**, 215501 (2017)
63. Z. Schwartzman-Nowik, E. Lerner, E. Bouchbinder, *Phys. Rev. E* **99**, 060601 (2019)
64. A. Barbot, M. Lerbinger, A. Lemaître, D. Vandembroucq, S. Patinet, *Phys. Rev. E* **101**, 033001 (2020)
65. E. Bitzek, P. Koskinen, F. Gähler, M. Moseler, P. Gumbsch, *Phys. Rev. Lett.* **97**, 170201 (2006)
66. J.F. Lutsko, *J. Appl. Phys.* **65**, 2991 (1989) □